

# Three-Dimensional Conjugate Tooth Surface Design and Contact Analysis of Harmonic Drive with Double-Circular-Arc Tooth Profile

chaosheng song (✉ [chaoshengsong@cqu.edu.cn](mailto:chaoshengsong@cqu.edu.cn))

Chongqing University <https://orcid.org/0000-0002-9547-0480>

**Feihong Zhu**

Chongqing University

**Xinzi Li**

Chongqing University

**Xuesong Du**

Chongqing University

**Zhifeng Liu**

Chongqing University

---

## Research Article

**Keywords:** Three-dimensional conjugate tooth surface, Coning deformation, Double-circular-arc tooth profile, Harmonic drive, Contact characteristics

**Posted Date:** March 14th, 2022

**DOI:** <https://doi.org/10.21203/rs.3.rs-1229849/v1>

**License:**   This work is licensed under a Creative Commons Attribution 4.0 International License.

[Read Full License](#)

---

# Three-dimensional conjugate tooth surface design and contact analysis of harmonic drive with double-circular-arc tooth profile

Chaosheng Song<sup>1</sup>, Feihong Zhu<sup>1</sup>, Xinzi Li<sup>1</sup>, Xuesong Du<sup>1</sup>, Zhifeng Liu<sup>2</sup>

<sup>1</sup> State Key Laboratory of Mechanical Transmissions, Chongqing University, Chongqing 400030, China

<sup>2</sup> Hangzhou Advance Gearbox Group Co., Ltd, Hangzhou 311203, China

Corresponding author: Chaosheng Song: Email: chaoshengsong@cqu.edu.cn

**Abstract:** A three-dimensional conjugate tooth surface design method of Harmonic drive with a double-circular-arc tooth profile is proposed. The radial deformation function of the flexspline (FS) obtained by FEA is introduced into the kinematics model, and the optimization of the overlapping conjugate tooth profile is completed by analyzing the FS tooth enveloping process. Considering the hobbing process, the three-dimensional machinable tooth surface of FS is obtained. Considering the coning deformation of the FS, the multi-section assembly and meshing motion simulation of machinable tooth surface are carried out. Finite element method is used to analyze and compare the loaded contact characteristics. Results show that the proposed design method can obtain an internal gear pair composed of a circular spline with a spur gear tooth surface and a FS with a machinable tooth surface. Under the rated torque, 24% of the FS teeth are engaged in meshing, and more than 4/5 of the tooth surface in the axial direction carries the load. The contact patterns, maximum contact pressure and transmission error of the machinable tooth surface are 227.2%, 40.67%, and 71.24% of the spur gear tooth surface respectively, showing excellent transmission performance.

**Keyword:** Three-dimensional conjugate tooth surface, Coning deformation, Double-circular-arc tooth profile, Harmonic drive, Contact characteristics

## 1 Introduction

Harmonic drive (HD) is mainly composed of flexspline (FS), circular spline (CS) and wave generator (WG). It is widely involved in aerospace, industrial robots and other fields due to the advantages of compact structure, large transmission ratio and high transmission precision. However, the elastic coning deformation of FS has spatial features, especially for the short-cup FS. To obtain ideal contact characteristics, the tooth surfaces of FS and CS need to be designed as spatially conjugate tooth surfaces. Therefore, it is of great significance to establish an HD kinematics model based on the coning deformation of FS, and design the three-dimensional (3D) conjugate tooth surface of FS.

Many researchers have carried out a lot of work in the field of HD structure design [1, 2], meshing theory [3-5], tooth profile design [5-9], backlash and meshing force distribution [10]. In terms of the design of HD conjugate tooth profile, Yang [11] et al. proposed an exact solution for two-dimensional conjugate profiles of zero-backlash HDs with elliptical cam WG. Dong [1, 4] et al. proposed an HD kinematics model considering the deformation of FS. They pointed out that one of the tooth surfaces of FS and CS must be a spatial tooth surface, otherwise it will cause unnecessary interference and deformation. Wu [12] et al. proposed that the tooth surface of CS adopts the spatial tooth surface, and that of the FS adopts the spur gear tooth surface. However, it is difficult to achieve mass production of CS spatial tooth surface. Considering the coning deformation of FS, Liu [13] et al. converted the design of the 3D tooth surface of CS into a 2D tooth profile design in multiple cross-sections. Wang [14] et al. discretized the FS tooth surface into many cross-sections normal to the rotating axis, and designed the FS tooth surface by reasonably adjusting the position of the FS tooth profile along the radius. Chen [15] et al. analyzed the spatial coning deformation features of the FS based on the straight generatrix assumption. In view of the problem that there is a certain deviation between the actual deformation and the assumed linear deformation, Li [16] uses the finite element method to explore the influence of the structural parameters on the radial deformation of FS. The tooth surface of the FS is modified based

on the simulation results of the FS deformation. The above papers mostly regard the tooth surface of the harmonic gear as a series of discrete cross-sectional tooth profiles to design the conjugate tooth surface. Some of them consider the influence of the FS coning deformation to design the tooth surface of harmonic gear. However, they failed to analyze the coning deformation of the FS in detail, and only qualitative conclusions can be drawn instead of quantitative results. Therefore, considering the manufacturing technology of FS and CS, analyzing the coning deformation of FS in detail, and proposing a 3D tooth surface design method that is more in line with engineering reality is of great significance.

This paper proposes a 3D conjugate tooth surface design method of HD with double-circular-arc tooth profile. The radial deformation function of the FS obtained by FEA is introduced into the kinematics model of HD. Considering the hobbing process of FS, the 3D conjugate tooth surface of FS is obtained by adjusting the position of the main section tooth profile along the radius direction. On this basis, considering the coning deformation of FS, the multi-section assembly and meshing motion simulation of the 3D conjugate tooth surface are carried out. Then, the finite element method is used to analyze and compare the loaded contact characteristics of the FS with spur gear tooth surface and 3D conjugate tooth surface.

## 2 Kinematics model of harmonic drive considering the coning deformation of FS

If the combined effect of complex factors such as the actual geometry of the flexible bearing and the transition fillet of the gear ring is considered, the kinematics of HD will be very complicated. Therefore, to simplify the problem, the following assumptions are made.

- (1) The displacement of the FS along the rotating axis direction is negligible [7].
- (2) There is a curved surface inside the thin-wall cylinder of the FS that cannot be elongated, which is called the FS neutral surface.
- (3) The elastic deformation state of the FS neutral surface is stable, ignoring the slight swing relative to the average position caused by the distribution of meshing gear teeth.
- (4) The intersected curve between the FS neutral surface and each cross-section normal to the rotating axis is the neutral curve in this section. The neutral curve on each section is not elongated and is a standard ellipse with different eccentricities.
- (5) The FS is manufactured in an undeformed state, and the FS teeth are regarded as rigid bodies connected by a flexible ring.

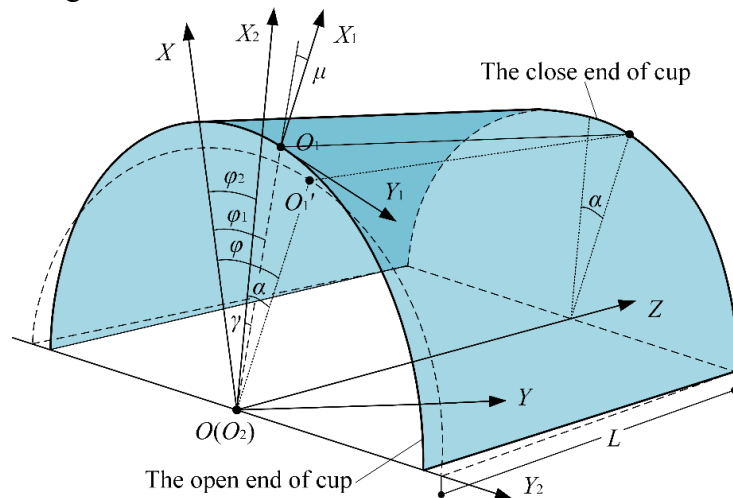


Fig.1 Coordinate systems of harmonic drive

As shown in Fig.1, the coning deformation of the FS is considered to establish an HD coordinate system. The CS is fixed, the WG is input, and the FS is output. The coordinate system  $S(O-XYZ)$  is fixedly connected to the WG, the  $Z$ -axis coincides with the rotating axis, and the  $X$ -axis is the major

axis of the WG. The coordinate system  $S_1(O_1-X_1Y_1Z_1)$  is fixedly connected to the FS tooth, the  $X_1$  axis is the symmetrical line of the FS tooth profile, and the origin  $O_1$  is the intersected point of the  $X_1$  axis and the FS neutral curve. The coordinate system  $S_2(O_2-X_2Y_2Z_2)$  is connected to the CS, and the  $Z$ -axis also coincides with the rotating axis. At the initial position, the coordinate system  $S$  and  $S_2$  coincide, the origin  $O_1$  is located at the vertex of the WG major axis, and the 3 axes  $X_1$ ,  $X_2$  and  $X$  are collinear. The WG rotates counterclockwise by angle  $\varphi_2$  relative to the  $X_2$  axis, the designated point  $O_1$  at the open end of the FS rotates clockwise by angle  $\gamma$ , and the closed-end rotates clockwise by angle  $\alpha$ . The WG forces the neutral curve of the FS to undergo elliptical deformation, so that the position of  $O_1$  point moves from  $O_1'$  to  $O_1$  in Fig.1, and the normal direction changes from  $OO_1'$  to  $X_1$  axis. After the WG is installed in the FS cylinder, the FS neutral curve on different sections normal to the rotating axis has different maximum radial displacements.  $a$  is the semi-length of the major axis of the neutral curve on each section of the FS, which can be expressed as a function of  $z$ .

$$a(z) = r_m + d_a(z) \quad (1)$$

where  $r_m$  is the radius of the FS neutral surface before deformation,  $d_a(z)$  is the function of the maximum radial displacement of the FS, which will be obtained by finite element analysis of the FS assembly deformation in Section 3.1.

The semi-length of the minor axis  $b$  can be determined according to the assumption (4).

$$b(z) = \frac{1}{9} \left\{ (12r_m - 7a(z)) + \left( 4\sqrt{a(z)(3r_m - 2a(z))} \right) \right\} \quad (2)$$

To facilitate elliptic integration, all kinematics parameters are expressed as a function of  $\varphi_1$ . According to the parametric equation of the standard ellipse, the polar radius of the neutral curve on each section can be expressed in polar coordinates as

$$r(\varphi_1) = r = \frac{a(z)b(z)}{\sqrt{a(z)^2 \sin^2 \varphi_1 + b(z)^2 \cos^2 \varphi_1}} \quad (3)$$

where  $r$  is the polar radius of  $OO_1$ .

According to the literature [11], the equations of the kinematic parameters and their derivatives in Fig.1 can be derived as follows

$$\frac{dr}{d\varphi_1} = \dot{r} = -\frac{a(z)\varepsilon^2 \sin\varphi_1 \cos\varphi_1}{(1 + \varepsilon^2 \sin^2 \varphi_1)^{\frac{3}{2}}} \quad (4)$$

$$\varphi = \frac{1}{r_m} \int_0^{\varphi_1} \sqrt{r^2 + \dot{r}^2} d\varphi_1 \quad (5)$$

$$\varphi_2 = \frac{Z_1}{Z_2 r_m} \int_0^{\varphi_1} \sqrt{r^2 + \dot{r}^2} d\varphi_1 \quad (6)$$

$$\mu = \arctan \frac{-\dot{r}}{r} = \arctan \frac{\varepsilon^2 \sin\varphi_1 \cos\varphi_1}{1 + \varepsilon^2 \sin^2 \varphi_1} \quad (7)$$

$$\gamma = \varphi_1 - \varphi_2 \quad (8)$$

$$\beta = \gamma + \mu \quad (9)$$

where  $\mu$  is the angle between the polar radius  $OO_1$  and the  $X_1$  axis.  $\varepsilon$  is the second eccentricity of the ellipse,  $\varepsilon = \sqrt{a(z)^2 - b(z)^2}/b(z)$ .

The coordinate system  $S_2$  shown in Fig.1 can be converted to  $S_1$ , the coordinate transfer matrix  $\mathbf{M}_{12}$  and the base vector transfer matrix  $\mathbf{W}_{12}$  can be expressed as follows

$$\mathbf{M}_{12} = \begin{bmatrix} \cos\beta & \sin\beta & -r\cos\mu \\ -\sin\beta & \cos\beta & r\sin\mu \\ 0 & 0 & 1 \end{bmatrix} \quad (10)$$

$$\mathbf{W}_{12} = \begin{bmatrix} \cos\beta & \sin\beta & 0 \\ -\sin\beta & \cos\beta & 0 \\ 0 & 0 & 1 \end{bmatrix} \quad (11)$$

According to the conjugate theory, the normal vector of the tooth surface and the relative velocity at the meshing contact point are perpendicular to each other. That is to say, the conjugation condition can be expressed as follows [11]

$$\mathbf{n}_i \cdot \mathbf{v}_i^{(12)} = 0 \quad (i = 0,1,2) \quad (12)$$

where  $\mathbf{n}_i$  is the normal vector of the contact point of two conjugate surfaces, and the subscript  $i$  represents the coordinate system  $S_i$ .  $\mathbf{v}_i^{(12)}$  is the relative velocity vector of the contact point.

In the coordinate system  $S_1$ , substituting  $\mathbf{n}_1 = \mathbf{W}_{12}\mathbf{n}_2$  and  $\mathbf{v}_1^{(12)} = \frac{d\mathbf{r}_1}{dt} = \frac{d\mathbf{M}_{12}}{dt}\mathbf{r}_2$  into Eq. (12), it can be transformed into

$$\mathbf{n}_1 \cdot \mathbf{v}_1^{(12)} = \mathbf{n}_2^T \mathbf{W}_{12}^T \frac{d\mathbf{M}_{12}}{dt} \mathbf{r}_2 = 0 \quad (13)$$

$$\mathbf{n}_2^T \Phi \frac{d\varphi_1}{d\varphi} \frac{d\varphi}{dt} \mathbf{r}_2 = \mathbf{n}_2^T \Phi \mathbf{r}_2 \frac{d\varphi_1}{d\varphi} = 0 \quad (14)$$

Here,

$$\Phi = \mathbf{W}_{12}^T \frac{d\mathbf{M}_{12}}{d\varphi_1} \quad (15)$$

Substituting  $\frac{d\mathbf{M}_{12}}{d\varphi_1} = \begin{bmatrix} -\dot{\beta}\sin\beta & -\dot{\beta}\cos\beta & r\dot{\mu}\cos\mu + \dot{r}\sin\mu \\ \dot{\beta}\cos\beta & -\dot{\beta}\sin\beta & r\dot{\mu}\sin\mu - \dot{r}\cos\mu \\ 0 & 0 & 0 \end{bmatrix}$  and  $\mathbf{W}_{12}^T = \begin{bmatrix} \cos\beta & \sin\beta & 0 \\ -\sin\beta & \cos\beta & 0 \\ 0 & 0 & 1 \end{bmatrix}$

into Eq. (15), then the following matrix can be obtained

$$\Phi = \begin{bmatrix} 0 & -\dot{\beta} & \dot{\beta}r\cos\gamma - \dot{r}\sin\gamma - \dot{\gamma}r\cos\gamma \\ \dot{\beta} & 0 & -\dot{\beta}r\sin\gamma - \dot{r}\cos\gamma + \dot{\gamma}r\sin\gamma \\ 0 & 0 & 0 \end{bmatrix} \quad (16)$$

In the cross-section where the  $Z$  coordinate value is  $z_i$ , the kinematic parameters and their derivatives are obtained according to Eqs. (1)~(9) and the maximum radial displacement function  $d_a(z)$ . The CS tooth profile curve  $\tilde{C}$  is expressed as a function of arc length  $s$ . For each point on the tooth profile curve  $\tilde{C}$ , there is a parameter value  $s_j(j=1, 2, \dots, s)$ . The vector  $\mathbf{r}_2$  and  $\mathbf{n}_2$  of each point are substituted into Eq. (13) to obtain the angle  $\varphi_1$  when this point performs conjugate motion, which is recorded as  $\varphi_{1j}(j=1, 2, \dots, s)$ . Substituting  $\varphi_{1j}$  into the following Eq. (17), the theoretical tooth profile curve  $\tilde{F}$  of the FS conjugated with the CS tooth profile curve  $\tilde{C}$  can be obtained.

$$\mathbf{r}_i^{(1)} = \mathbf{M}_{12} \cdot \mathbf{r}_i^{(2)} \quad (i = 0,1,2) \quad (17)$$

### 3 Solution of three-dimensional conjugate tooth surface design

To analyze the elastic coning deformation of the FS in detail, the finite element method is used to study the deformation of the FS under the action of the WG. The design parameters of HD are shown in Table 1. Fig.2 shows the double-circular-arc tooth profile with common-tangent, and Table 2 shows the specific tooth profile parameters.

Table 1 Design parameters of harmonic gear

Parameter	Value	Parameter	Value
-----------	-------	-----------	-------

Transmission ratio $i$	50	Modulus $m$ (mm)	0.5
Tooth number of FS $Z_1$	100	Rated torque $T$ (Nm)	33
Tooth number of CS $Z_2$	102	Radial deformation coefficient $d_{a0}^*$	0.88

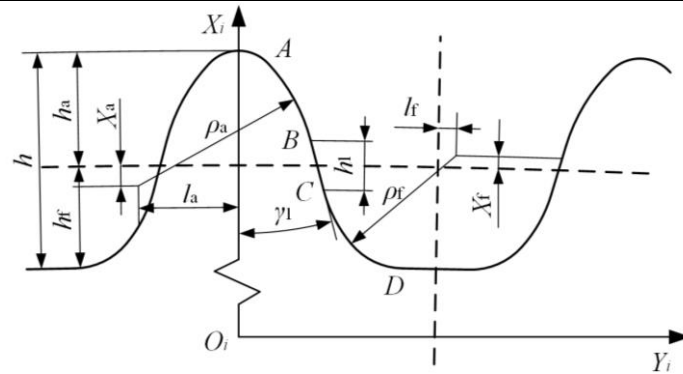


Fig.2 The schematic diagram of double-circular-arc tooth profile with common-tangent

Table 2 Tooth profile parameters of HD

	Parameter	FS	CS	[Units]
AB arc	X axis offset $x_a$	0.1630	0.2489	mm
	Y axis offset $y_a$	-0.3450	0.4463	mm
	Radius $r_a$	0.6342	0.74	mm
BC arc	Longitudinal length $h_l$	0.2456	0.26	mm
	Obliquity angle $\gamma_l$	29.6715	30	deg
CD arc	X axis offset $x_r$	0.1303	-0.0236	mm
	Y axis offset $y_r$	-0.0249	-0.1745	mm
	Radius $r_r$	0.5011	0.31	mm

### 3.1 Analysis of coning deformation of flexspline

Fig.3 shows the finite element model of the FS coning deformation considering the specific structure of the flexible bearing.

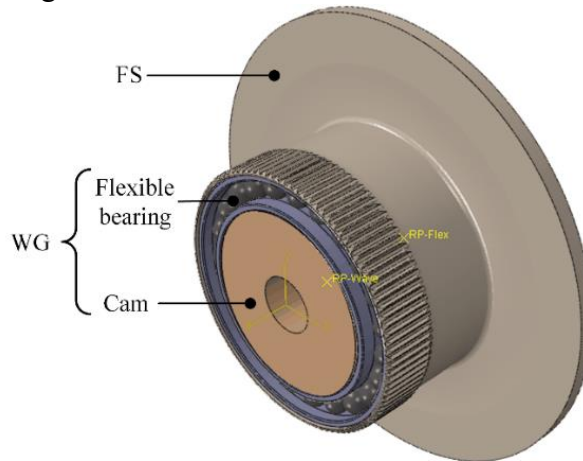


Fig.3 Finite element model of flexspline coning deformation

The model is jointly established by HyperMesh and Abaqus. All components are considered as flexible bodies, and the mesh of each component is shown in Fig.28. The end face of the FS flange and the inner hole of the WG cam constrain all degrees of freedom. The tie constraint between the inner race and the rollers of the flexible bearing ensures the positions of the rollers and avoids rigid body displacement [17]. All other contact pairs adopt surface-to-surface contact. The friction coefficient between the rollers and the outer race is 0.02 [3], and that of the remaining contact pairs are 0.15 [18]. The material properties are shown in Tab.3. The elliptical cam and the inner race have an interference fit, and the cam automatically adjusts the initial interference to cause the deformation of the flexible

bearing and the FS, to realize the assembly simulation of the flexspline. Fig.4 shows the assembly displacement distribution of the FS. The open end of the FS has the largest radial displacement, and the close-end has almost no deformation, which shows as a coning deformation. The FS teeth have an outward inclination angle  $\theta_1$  at the major axis, and an inward inclination angle  $\theta_2$  at the minor axis. In this paper, the cross-section where the WG is located is defined as the main section (design section).

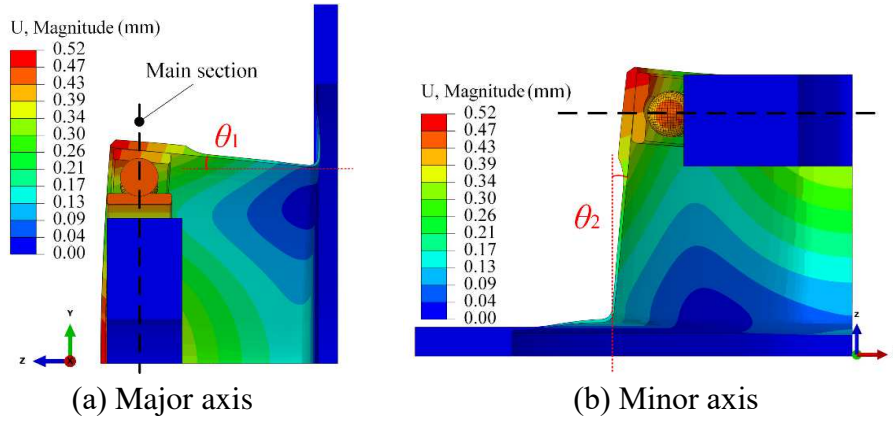


Fig.4 The assembly deformation of flexspline cylinder

To extract the detailed data of the FS coning deformation, 41 circular paths are established on the FS neutral surface. The circular path is evenly distributed along the rotating axis. As shown in Fig.5, the  $0^\circ$  polar axis is at the minor axis of the WG, and the counterclockwise direction is positive.

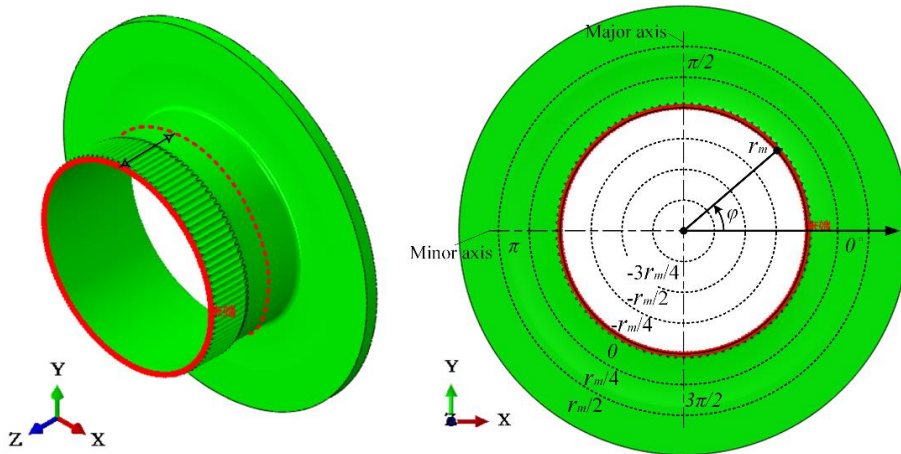


Fig.5 Circular path on flexspline neutral surface

Figs. 6~8 show the radial deformation, tangential deformation and axial deformation distribution of the opening part on the FS neutral surface. The above 3 kinds of deformations distribution have obvious periodicity, and the values are positive and negative. The radial deformation has obvious conical characteristics along the rotating axis, tilting outward at the major axis and tilting inward at the minor axis. The maximum and minimum values are 0.511mm and  $-0.501$ mm, respectively. The tangential deformation value has a conical characteristic along the rotating axis, and the absolute value between the major axis and the minor axis is relatively large, and the value at the major and minor axis is close to zero. The maximum and minimum values are 0.258mm and  $-0.255$ mm, respectively. Taking the Z-axis direction in Fig.5 as positive, the maximum value of axial deformation is 0.146mm at the minor axis, and the minimum value is  $-0.101$ mm at the major axis. The conical characteristic is not obvious. Among the three deformations, the radial deformation has the largest value, the tangential deformation is the second, and the axial deformation is the smallest, and all have obvious conical characteristics except for the axial deformation.

The axial deformation of the FS neutral surface is relatively small compared to the radial and tangential deformation, and only affects the stress distribution of the shell, but does not affect the

kinematics of the harmonic drive [1]. Therefore, the axial deformation is ignored. Based on the extracted detailed data of the neutral surface deformation, the method in [19] is used to perform ellipse fitting on the neutral curve data of each cross-section. According to the ellipse fitting result, the maximum radial displacement on each cross-section of the FS neutral surface is obtained as the blue data points in Fig.9 (a). The maximum radial displacement is basically linear with the  $Z$  coordinate. The farther from the open end of the FS cup, the smaller the displacement, which is consistent with the experimental results in the literature [1]. Straight-line fitting is performed on the maximum radial displacement data, and the fitting straight line and fitting error are shown in Fig.9 (a) and (b).

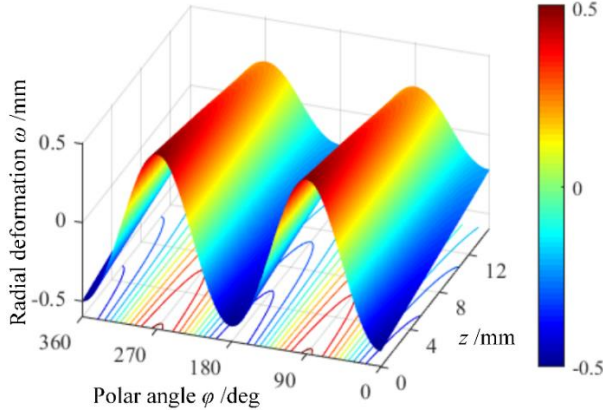


Fig.6 The radial deformation

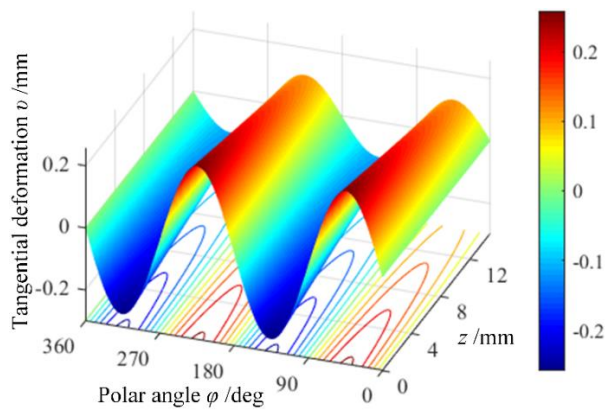


Fig.7 The tangential deformation

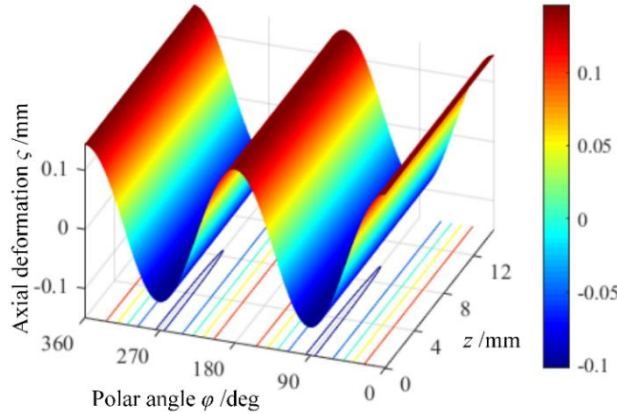
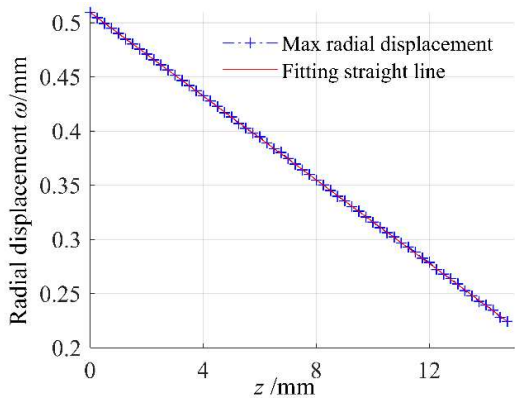
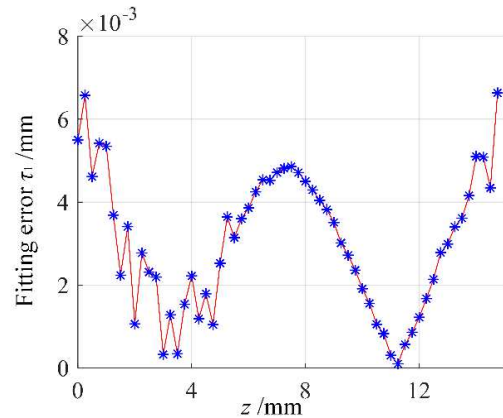


Fig.8 The axial deformation



(a) Straight-line fitting of max radial displacement



(b) Fitting error

Fig.9 Straight-line fitting and fitting error of maximum radial displacement

The maximum radial displacement function of the FS neutral surface obtained by straight-line fitting is as follows

$$d_a(z) = kz + c \quad (18)$$

where  $z$  is the axial coordinate value of each section,  $k=0.0185953$ ,  $c=0.5102824$ .

### 3.2 Analysis of conjugate existent domain and conjugate tooth profile

At present, the processing technology of the CS is mainly gear shaping and wire-cut electrical discharge machining. It is difficult and not economical to manufacture complex 3D tooth surfaces on CS. Therefore, the CS tooth is spur gear, and the FS tooth is the spatial tooth surface conjugated with the CS tooth surface. In the coordinate system  $S_2$ , the FS gear part is equally divided into 41 sections along the rotating axis, and the cross-sections from the 1st to the 41st correspond to  $z=0, 0.3, 0.6, \dots, 12$ , respectively. The main section corresponds to  $z=4\text{mm}$ .

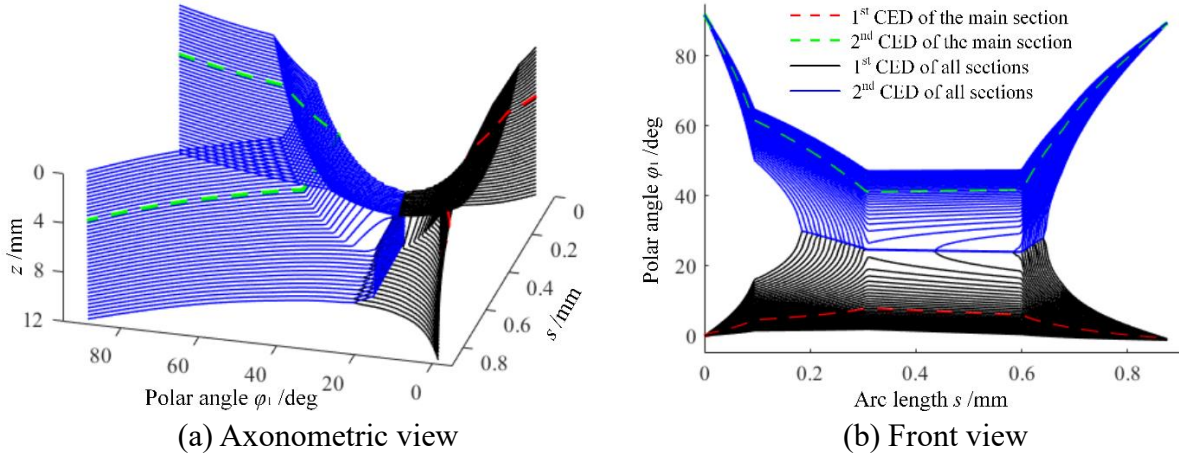


Fig.10 Conjugate existent domain of the CS with spur gear tooth surface

Fig.10 (a) and (b) are the axonometric view and the front view of the conjugate existent domain (CED), respectively. The bold dashed line indicates the two CEDs on the main section, and the solid line represents the CED of all other sections. The red/ black one is 1<sup>st</sup> CED, and the green/ blue one is 2<sup>nd</sup> CED. The angle range of the 1<sup>st</sup> CED on the main section is  $[-1.245^\circ, 7.34^\circ]$ , and that of the 2<sup>nd</sup> CED is  $[41.995^\circ, 91.834^\circ]$ . The angle ranges covered by the 1<sup>st</sup> and 2<sup>nd</sup> CED on all sections are  $[-1.245^\circ, 29.931^\circ]$  and  $[23.931^\circ, 91.834^\circ]$ , respectively. The expansion of the maximum angle range of the 1<sup>st</sup> and 2<sup>nd</sup> CED of the entire FS is 263.1% and 36.245% of the main section, respectively. The above analysis shows that the 1<sup>st</sup> CED of the entire FS gear part is 3.631 times the main section, which significantly increases the 1<sup>st</sup> CED. More gear teeth participate in meshing, which is of great significance for improving the transmission precision and torsional stiffness of HD. Substituting the CED into Eq. (17), the initial tooth surface of the FS conjugated to the CS tooth profile can be obtained. Since there are two CEDs, each section has two FS tooth profiles, as shown in Fig.11.

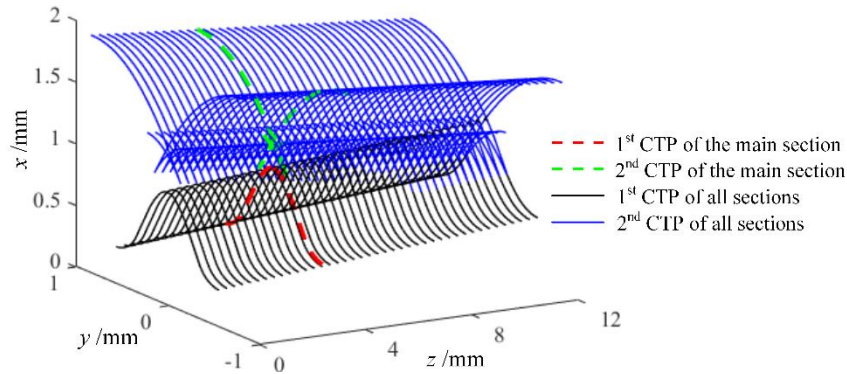


Fig.11 Initial tooth surface of the flexspline

The bold dashed line indicates the FS tooth profile on the main section, the red one is the 1<sup>st</sup> conjugate tooth profile (CTP), and the green one is the 2<sup>nd</sup> CTP. The two tooth profiles on the main section are separated from each other and do not cross each other, but only one of them is feasible. The solid line represents the CTP of all other sections, the black one represents the 1<sup>st</sup> CTP, and the blue one represents the 2<sup>nd</sup> CTP. The line type and color correspond to the CED in Fig.10. Figs. 10 and 11

show that the overlap of the CEDs occurs on a part of the section due to the effect of the coning deformation of FS. To analyze the overlapping phenomenon in detail, the movement trail of the CS tooth space relative to the tooth profile of the FS is calculated based on the kinematics model of HD in Section 2. It must be pointed out that the FS tooth profile on all 41 sections will form a 3D FS tooth surface to ensure the accuracy of the desired tooth surface. However, due to a large number of cross-sections, the results of 4 typical cross-sections are used to explain in detail. The Z coordinates of the 4 typical cross-sections in the coordinate system  $S_2$  are  $z=0, 4, 8,$  and  $12$ .

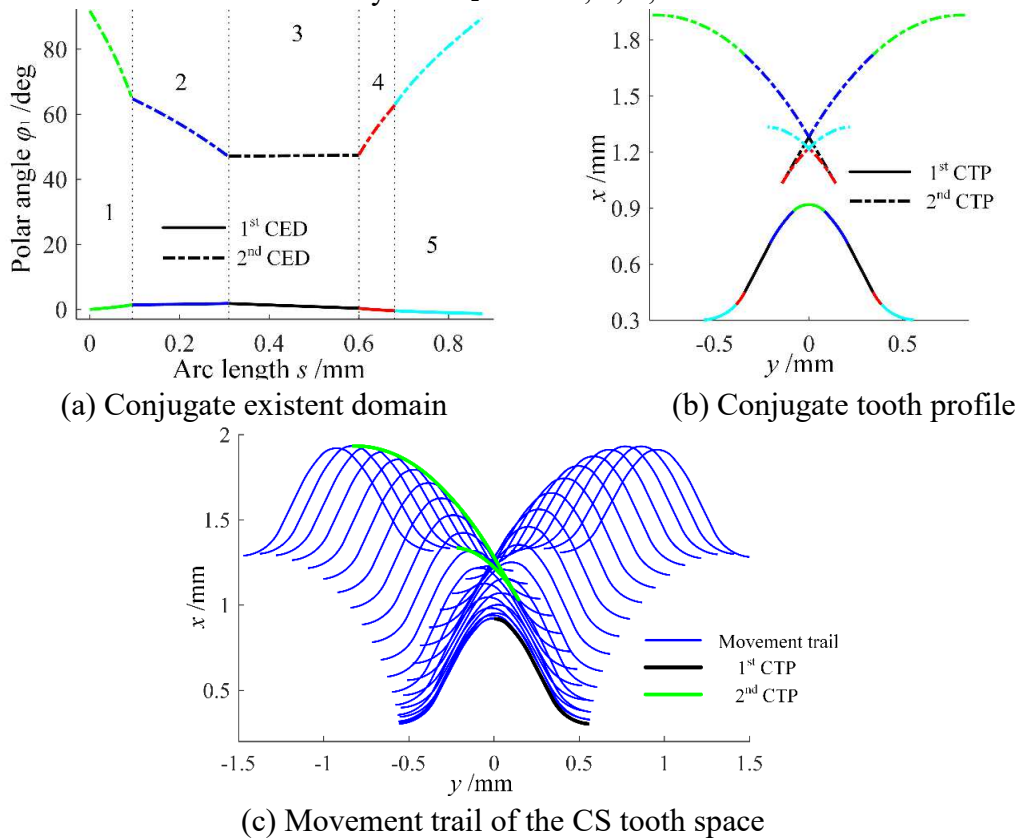
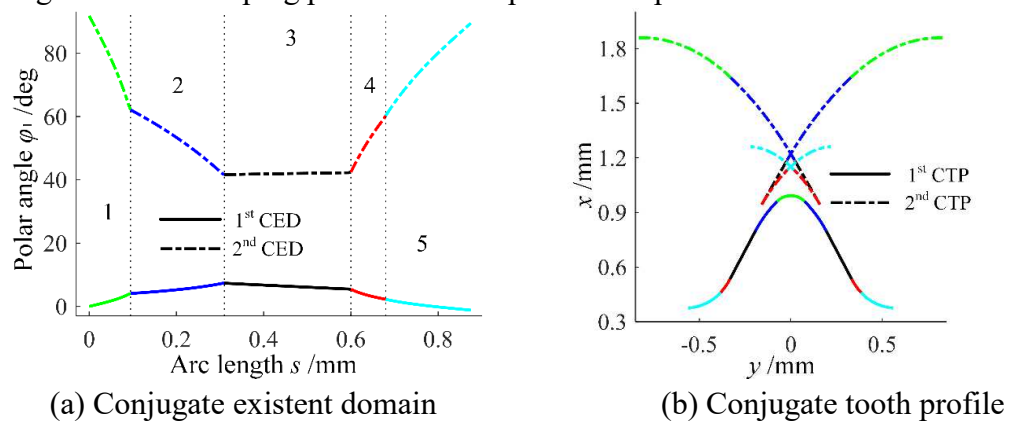
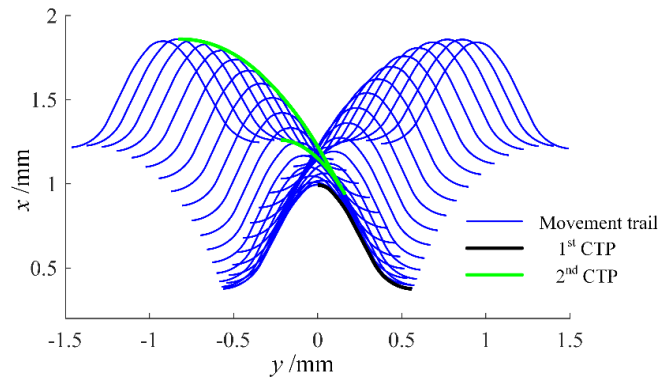


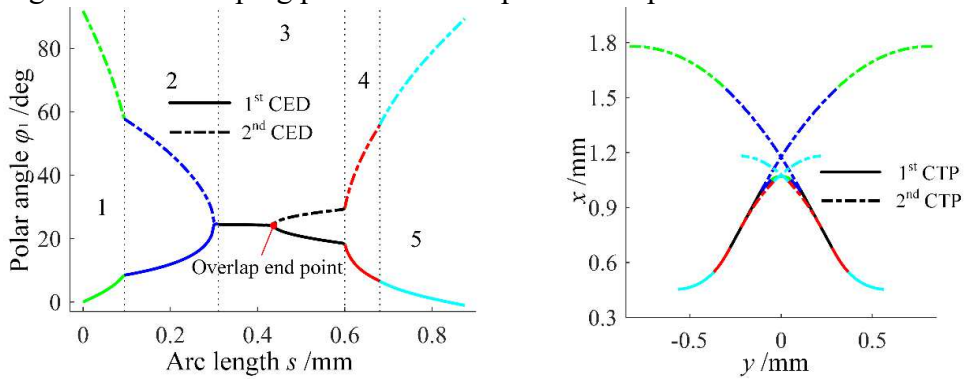
Fig.12 The enveloping process of flexspline tooth profile at  $z=0$ mm section





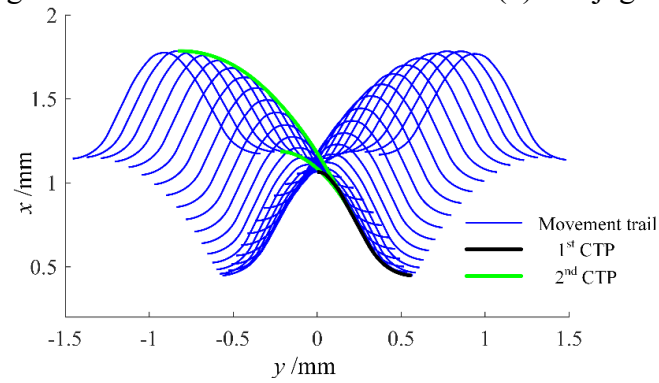
(c) Movement trail of the CS tooth space

Fig.13 The enveloping process of flexspline tooth profile at  $z=4\text{mm}$  section



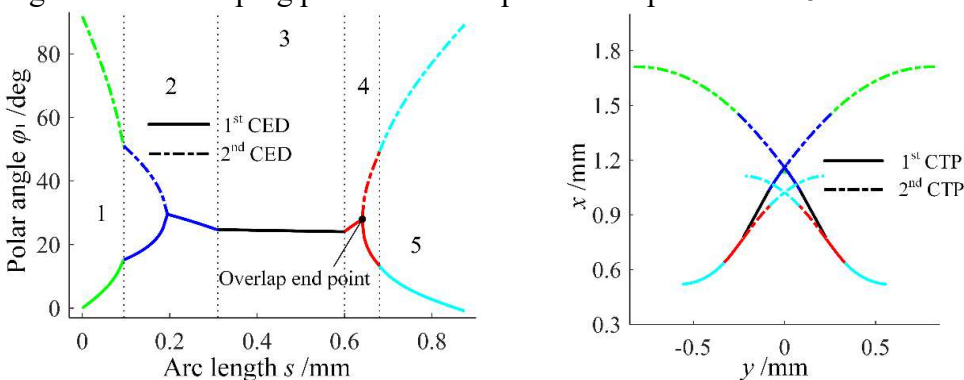
(a) Conjugate existent domain

(b) Conjugate tooth profile



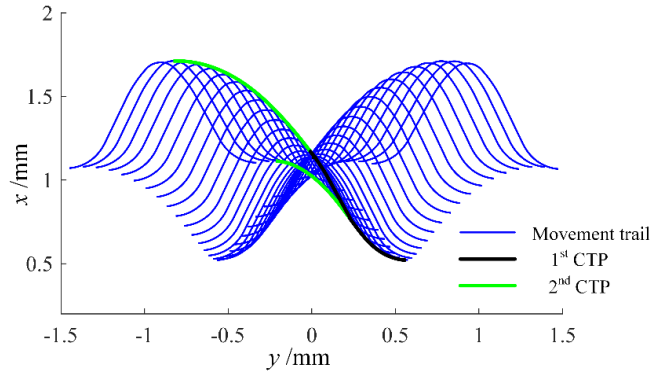
(c) Movement trail of the CS tooth space

Fig.14 The enveloping process of flexspline tooth profile at  $z=8\text{mm}$  section



(a) Conjugate existent domain

(b) Conjugate tooth profile



(c) Movement trail of the CS tooth space

Fig.15 The enveloping process of flexspline tooth profile at  $z=12\text{mm}$  section

Figs. 12 to 15 (a) and (b) are front views of the CED and CTP of 4 typical cross-sections. Among them: 1 tip transition arc (green), 2 addendum circular arc (blue), 3 common-tangent segment (black), 4 dedendum circular arc (red), 5 root transition arc (sky blue). Figs. 12~15 show that as the Z coordinate increases, the radial displacement of the FS neutral curve decreases, causing the two CEDs and the two CTPs to gradually approach each other and then overlap. When two CEDs overlap on a certain cross-section, the two CTPs on the same section will also overlap. The overlap of the CED starts from the common-tangent segment and extends to the addendum circular arc and the dedendum circular arc. Finally, the overlapping arc length of the CED accounts for 51% of the total arc length, which is more than half. The solved 1<sup>st</sup> and 2<sup>nd</sup> CTPs of the FS are formed by the envelope of CS tooth space at different positions. The CED of the 1<sup>st</sup> CTP is near  $0^\circ$ . At this position, the tooth pairs of the CS and the FS are in full engagement. The CED of the 2<sup>nd</sup> CTP is distributed in a wide range around  $\pm 90^\circ$ . At this position, the tooth pairs of the CS and the FS are in the engage-in or engage-out state.

### 3.3 Optimization of initial tooth surface of the FS

Figs. 12~15(c) show that as the Z coordinate increases, the 1<sup>st</sup> and 2<sup>nd</sup> CTPs firstly separate from each other, then gradually approach, and finally overlap each other, which introduces uncertain factors to the determination of the available CTP. When the two CTPs do not overlap or intersect, the 1<sup>st</sup> CTP is used as the available CTP, as shown in Figs. 12 and 13. However, when the two CTPs are overlapping and intersecting, if the 1<sup>st</sup> CTP is used as the available CTP, it will cause greater meshing interference, as shown in Figs. 14 and 15. In such a section, a part of the 2<sup>nd</sup> CTP appears inside the 1<sup>st</sup> CTP, and the available CTP should be composed of the 1<sup>st</sup> and 2<sup>nd</sup> CTPs, as shown in Figs. 16 and 17.

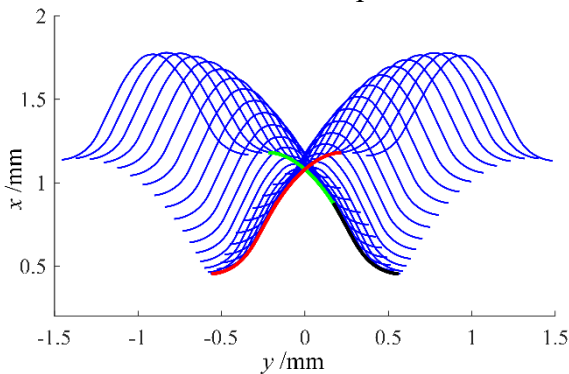


Fig.16 The available CTP at  $z=8\text{mm}$  section

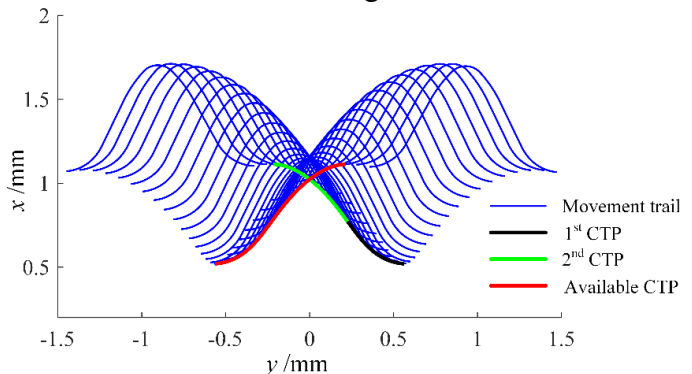


Fig.17 The available CTP at  $z=12\text{mm}$  section

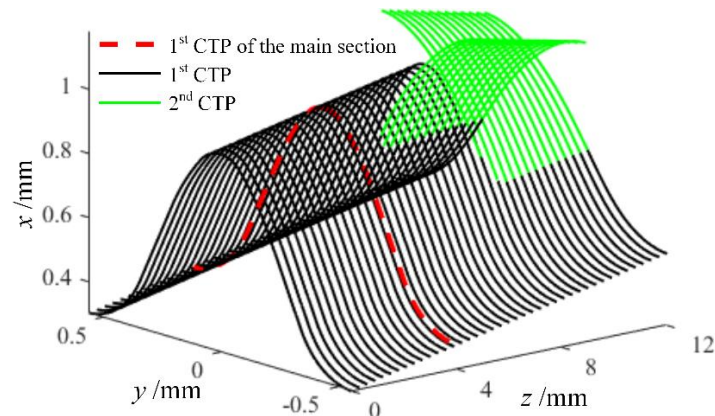


Fig.18 The available tooth surface of flexspline

Comparing Figs. 14, 15 with Figs. 16, 17, on the cross-section where the two CEDs overlap, the 1<sup>st</sup> and 2<sup>nd</sup> CTPs of the CS tooth profile segment after the overlap endpoint together constitute the available CTP. That is, the available CTP of the FS on this cross-section is formed by the envelope of the CS tooth tip. To eliminate unnecessary meshing interference, on the cross-section where the two CTPs overlap and intersect, the method shown in Figs. 16 and 17 are used to determine the available tooth profile in this section. Due to a large number of the cross-sections, Matlab code was written to calculate the available tooth profile on each section. Fig.18 shows the available FS tooth surface calculated by Matlab code, and the specific calculation process is as follows:

- (1) On a certain cross-section, subtract the value of the 2<sup>nd</sup> CED from that of the 1<sup>st</sup> CED.
- (2) Determine whether the two CEDs overlap, if the result is NO, the 1<sup>st</sup> CTP is used as the available tooth profile, if the result is YES, go to the next step.
- (3) Find the endpoint of the overlapping part, and the CTP determined jointly by the 1<sup>st</sup> and 2<sup>nd</sup> CEDs after the overlap endpoint is used as the available tooth profile.

At present, the manufacturing technology of the FS teeth in the HD mainly adopts gear hobbing. The available tooth surface of FS shown in Fig.18 has complex geometric features, and the tooth profile on each section along the axial direction is different, making the manufacture of the tooth surface very difficult. Therefore, considering the economy and feasibility, the machinable tooth surface is obtained by applying the tooth profile on the main section to all sections, and then reasonably adjusting the position of the tooth profile along the radius. The designed machinable tooth surface retains the geometric features of the available tooth surface as much as possible.

On all sections, the reasonable adjustment of the radial position satisfies the following 2 constraints:

- (1) To avoid the meshing interference of the gear pairs of the FS and the CS, it is necessary to ensure that the machinable tooth profile is located inside the available tooth surface area.
- (2) To retain the geometric features of the available tooth surface as much as possible, it must be ensured that part of the machinable tooth profile coincides with the available tooth surface.

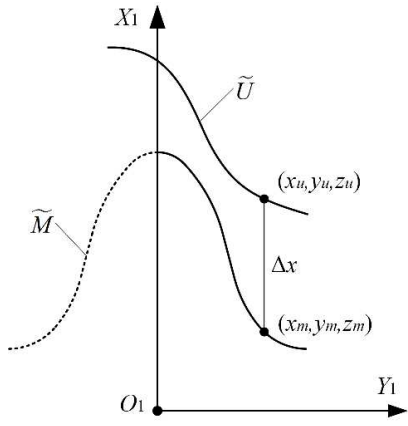


Fig.19 The radial movement  $\Delta h$

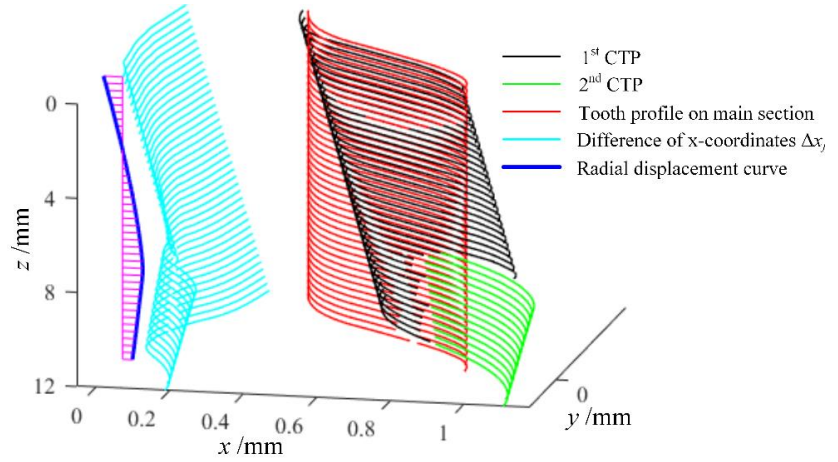


Fig.20 The schematic diagram of displacement calculation

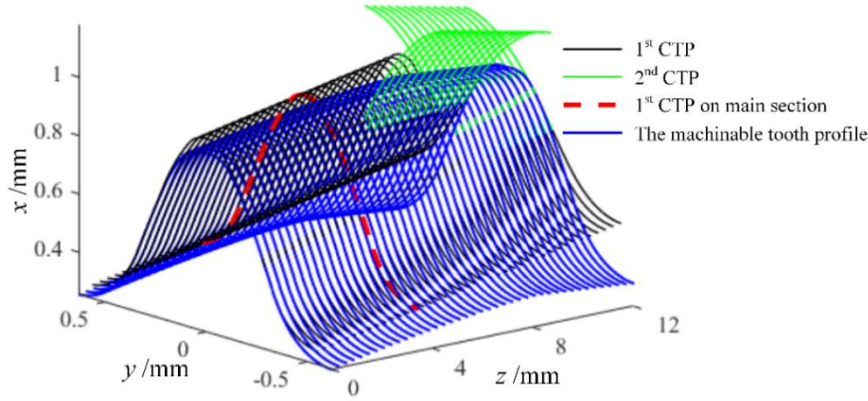


Fig.21 The machinable conjugate tooth surface of flexspline

The available tooth profile coordinates on each section minus the coordinates of the tooth profile on the main section, to obtain the radial movement  $\Delta h$  that satisfies the above two constraints. Fig.19 shows that  $\tilde{U}$  is the available tooth profile on any section,  $\tilde{M}$  is the tooth profile on the main section, and the coordinates of a point on  $\tilde{U}$  and  $\tilde{M}$  are  $(x_u, y_u, z_u)$  and  $(x_m, y_m, z_m)$ , respectively. On any section,  $z_u = z_m$  is satisfied, when  $y_{uj} = y_{mj}$ ,  $\Delta x_j = x_{uj} - x_{mj}$ , then  $\min(\Delta x_j)$  ( $j=1, 2, \dots, s$ ) is taken as the radial displacement  $\Delta h$  on this section. Fig.20 shows the calculation results of the radial displacement  $\Delta h$  on all sections. Fig.21 shows that the tooth profile on each cross-section of the machinable tooth surface is the same, which can be directly manufactured by the gear hobbing.

### 3.4 Modeling of the FS with machinable tooth surface

Because of the different radial displacements on each cross-section of the machinable tooth surface, it is difficult to establish an accurate 3D model only in CAD software. The author combined Matlab and Solidworks to realize the accurate establishment of the 3D model of the FS with the machinable tooth surface. The main steps are as follows:

(1) Use the Curve Fitting Tool in Matlab to fit the radial displacement data on all sections of the machinable tooth surface, as shown in Fig.22. To ensure the accuracy of the fitting, the 8th-degree polynomial fitting is used, and the curve fitting expression is as follows:

$$F(z) = p_1 z^8 + p_2 z^7 + p_3 z^6 + p_4 z^5 + p_5 z^4 + p_6 z^3 + p_7 z^2 + p_8 z + p_9 \quad (19)$$

where  $p_1 = -5.355 \times 10^{-8}$ ,  $p_2 = 2.414 \times 10^{-6}$ ,  $p_3 = -4.33 \times 10^{-5}$ ,  $p_4 = 0.0003955$ ,  $p_5 = -0.001963$ ,  $p_6 = 0.005185$ ,  $p_7 = -0.007033$ ,  $p_8 = 0.02118$ ,  $p_9 = -0.052$ .

(2) Input Eq. (19) into Solidworks, draw the 2D tooth profile of the FS on the main section, and use the "sweep" command to draw the machinable tooth surface of the FS, as shown in Fig.23.

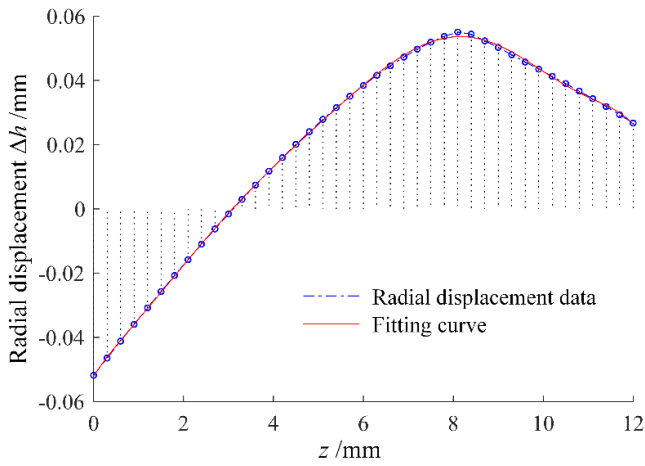


Fig.22 Radial displacement data

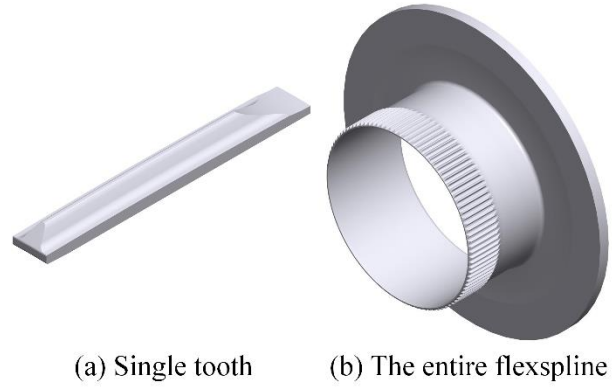


Fig.23 Three-dimensional model of the FS

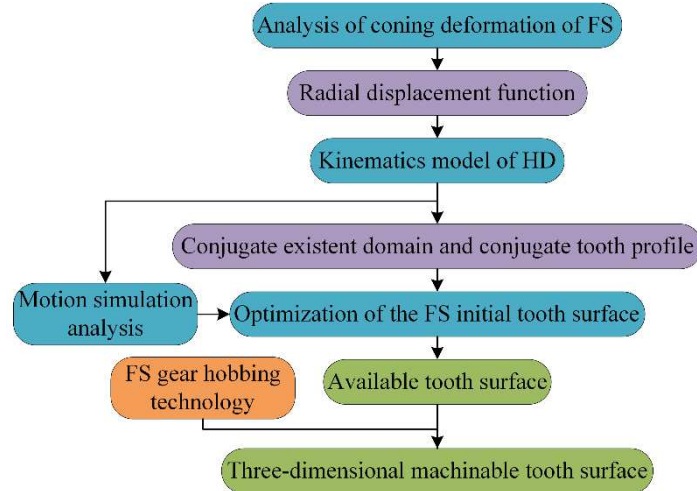


Fig.24 Frame diagram of the design method

In summary, this paper proposes a design method for the 3D tooth surface of FS. The radial deformation function of the FS obtained by FEA is introduced into the kinematics model of HD, and the overlapping CTP is optimized by analyzing the FS tooth enveloping process. Considering the hobbing process of the FS, the machinable tooth surface of FS is obtained by adjusting the position of the main section tooth profile along the radius direction. The specific process is shown in Fig.24.

#### 4 Motion simulation analysis

To evaluate the rationality and superiority of the designed 3D conjugate tooth surface, the multi-section assembly and meshing motion simulation of the machinable tooth surface are carried out. Fig.25 shows the assembly simulation results on 4 typical cross-sections of the machinable tooth surface. At the major axis of the WG, teeth 1 to 3 are in full engagement, and teeth 25 to 26 at the minor axis are completely disengaged. Affected by the coning deformation of the FS, in the fully engaged state, the tooth profile on the section near the closed end ( $z=12\text{mm}$ ) is at the innermost side, and the tooth profile on the open end section ( $z=0\text{mm}$ ) is at the outermost side. In the disengaged state, the position of the tooth profile on the two sections is just exchanged.

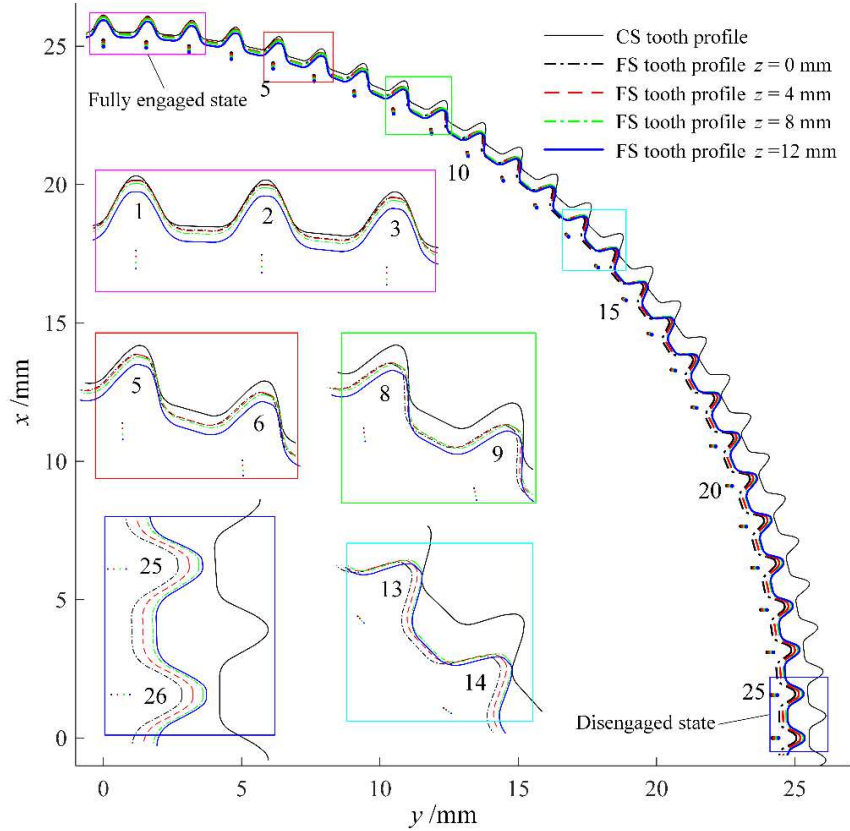


Fig.25 Assembly state diagram of machinable tooth surface

Figs. 26 show the meshing motion simulation results on 4 typical cross-sections of the machinable tooth surface. The red curve represents the movement trail of the origin  $O_1$  fixedly connected with the FS tooth. When the WG rotates  $360^\circ$ , the FS rotates two more teeth relative to the CS. In the process of gear tooth meshing, there is no meshing interference between CS and FS gear teeth, and part of the tooth profile on each section is always in the meshing contact state. From the section on the open end to the section on the closed end, the movement trail of the FS teeth gradually tends to be smooth, and the radial displacement is gradually reduced, which is consistent with the actual situation. On the section near the closed end, the tooth pair of the FS and the CS only meshes at the top of the tooth profile. On the remaining sections, the tooth pairs of the FS and the CS always maintain a continuous meshing with a large arc length. Fig.27 shows the backlash distribution on 4 typical cross-sections of the machinable tooth surface. The abscissa represents the number of teeth. The FS tooth at the major axis of the WG is marked as 1, and the other teeth are marked as 2, 3, 4, ...,  $n$  in the clockwise direction. The ordinate represents the backlash, and if there is tooth profile interference, the backlash is negative. The backlash distribution on 4 typical cross-sections is drawn with different line types. Take the backlash value less than 0.003mm as the possible condition for meshing contact [20], and mark the backlash value involved in the meshing with a red circle. The results show that some of the gear teeth on each section of the FS are engaged in meshing. The number of gear teeth participating in the meshing from the section  $z=0\text{mm}$  to the section  $z=12\text{mm}$  are 3 (1st~3rd), 5 (1st~5th), 11 (3rd~13th), and 5 (9th~14th) respectively, and the gear teeth involved in meshing gradually move away from the major axis. Although the backlash distribution on each section is different, the overall backlash distribution of the FS made up of all sections is more uniform and the fluctuation is small.

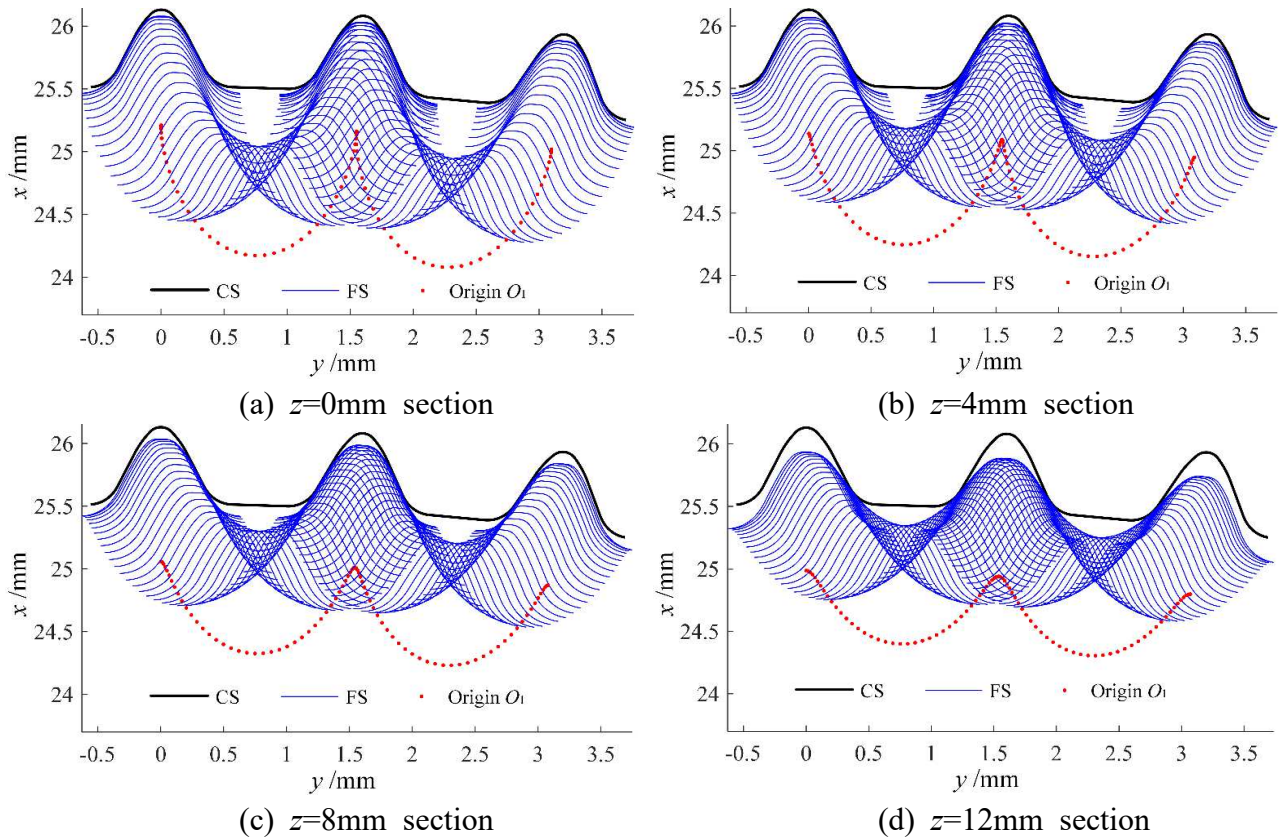


Fig.26 The relative movement trail of FS tooth profile on 4 typical cross-sections

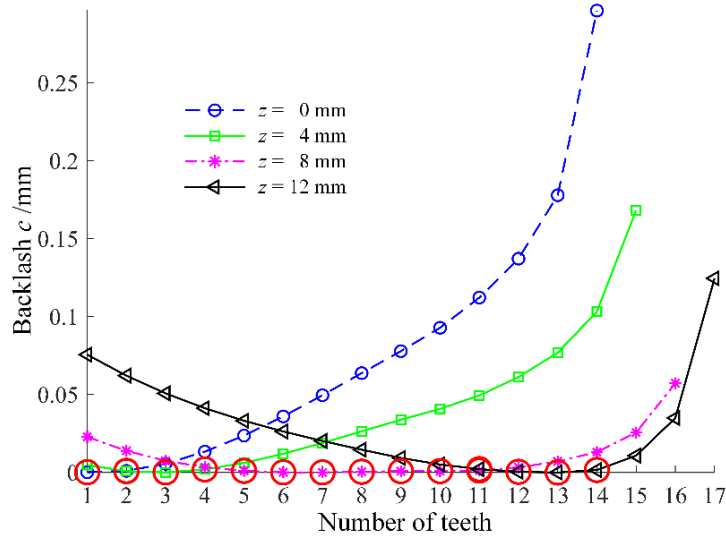


Fig.27 The distribution of minimum backlash

### 5 Loaded tooth contact analysis

The finite element model of the loaded harmonic gear contact analysis is established by adding the CS component to the finite element model of the FS coning deformation in section 3.1. All parts are divided into hexahedral element shape, as shown in Fig.28. The material properties are shown in Table 3. Three reference points RP-Wave, RP-Flex and RP-Rigid are established, which are coupled to the inner wall of the WG cam, the end face of the FS flange and the outer wall of the CS respectively. The analysis steps are set as follows:

(1) Fix all the degrees of freedom of the 3 reference points RP- $i$  ( $i$ =Wave, Flex, Rigid), and the cam automatically adjusts the initial interference to cause the flexible bearing and the FS to deform to realize the assembly of the flexspline.

(2) A surface-to-surface contact is established between the tooth surface of the FS and CS, and the

friction coefficient is 0.15.

(3) The rotational freedom of reference point RP-Flex is released, and a counterclockwise torque of 33Nm is applied to realize FS loading.

(4) The rotation displacement in the counterclockwise direction is applied to the reference point RP-Wave to realize the FS rotation driven by the WG.

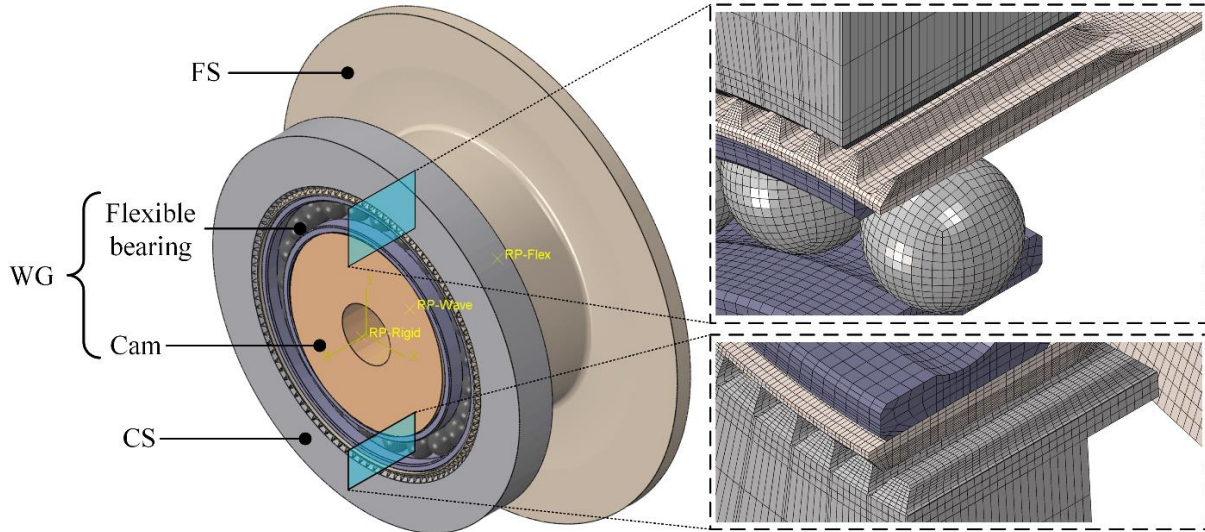


Fig.28 The finite element model of the loaded harmonic gear

Table 3 Material mechanics properties of parts of HD

Parameter	Material	Young's modulus $E$	Poisson's ratio $\nu$
FS	30CrMnNi	196	0.3
CS	QT400	130	0.27
WG	GCr15	208	0.3
[Units]	\	GPa	\

Fig. 29 (a) and (b) respectively show the contact pressure distribution in the meshing area of the FS with spur gear tooth surface and the 3D machined tooth surface. The FS with spur gear tooth surface has 7 teeth on one side (14 on both sides) to engage in meshing, accounting for 14%. The contact patterns are mainly concentrated at the edge of the opening end, and the maximum contact pressure appears on the 6<sup>th</sup> tooth, with a value of 1256.5 MPa. The FS with the 3D machinable tooth surface has 12 teeth on one side (24 on both sides) to engage in meshing, accounting for 24%. More than 4/5 tooth surfaces in the tooth width direction are engaged in meshing, and the meshing condition is good. The maximum contact pressure appears on the 8<sup>th</sup> tooth.

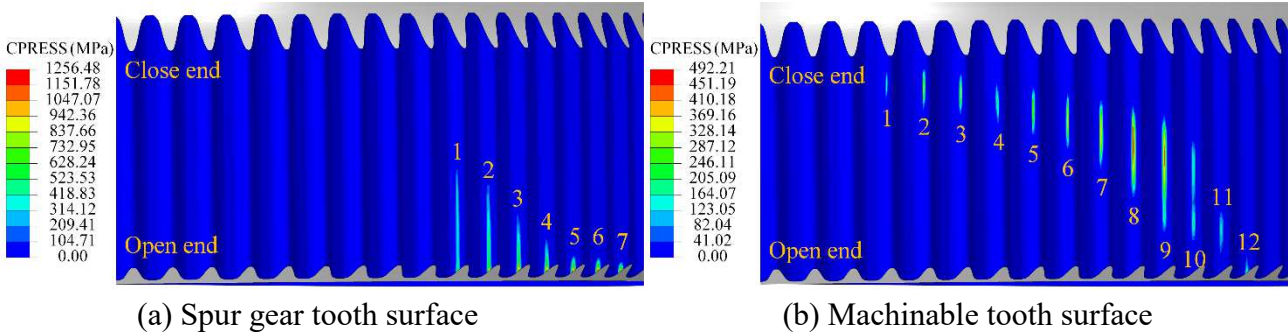


Fig.29 Contact pressure distribution in the meshing area of the FS

Fig. 30 shows the maximum contact pressure distribution of the contacting gear teeth of the FS with a spur gear tooth surface and a 3D machinable tooth surface. The 3D machinable tooth surface has more teeth involved in meshing than the spur gear tooth surface, and the load distribution between the teeth is more uniform and the value is smaller.

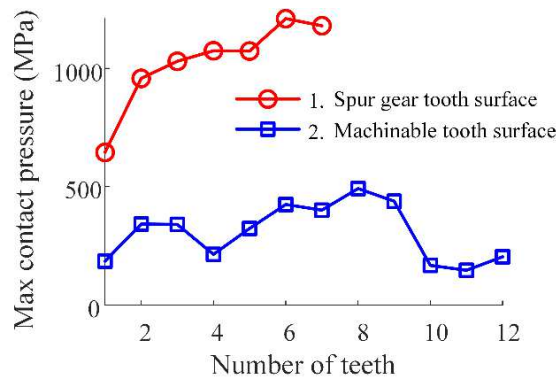


Fig.30 Max contact pressure distribution of the contacting gear teeth of the FS

Fig. 31 shows the contact pattern of FS with a spur gear tooth surface and a 3D machinable tooth surface. The FS with spur gear tooth surface is in contact at the edge of the opening end. The contact pattern accounts for 16.46% of the full tooth surface, and the maximum contact pressure is 1210.14 MPa. The full tooth width direction of the FS with the 3D machinable tooth surface basically participates in meshing. The contact pattern accounts for 37.40% of the full tooth surface, which is 2.272 times that of the spur gear tooth surface. The main contact area is in the middle of the tooth width, and the maximum contact pressure (492.16 MPa) is only 40.67% of the spur gear tooth surface. Fig. 32 shows the transmission error of a harmonic gear with a spur gear tooth surface and a 3D machinable tooth surface during the 180° rotation of the WG. Fig. 33 shows the peak-to-peak value of transmission error (TE).

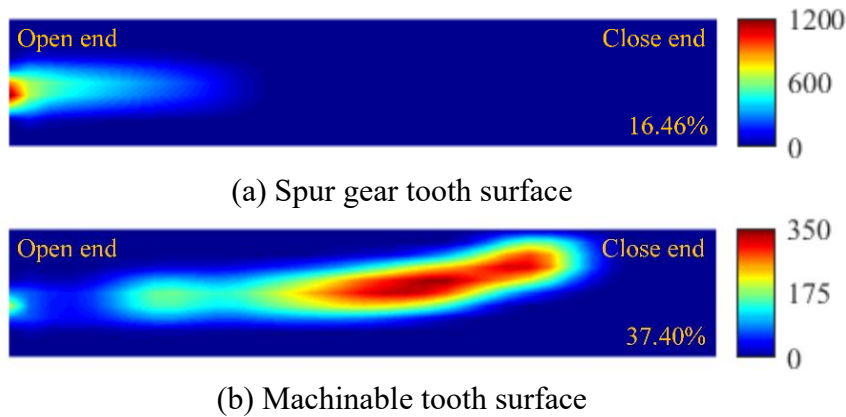


Fig.31 Contact pattern of flexspline

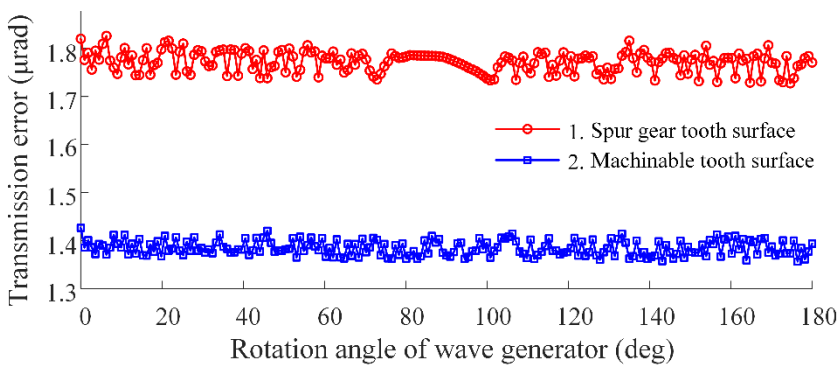


Fig.32 Transmission error

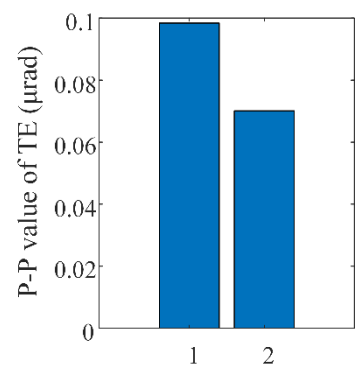


Fig.33 P-P value of TE

The results show that the transmission errors of the two tooth surfaces have no long-period TE. The peak-to-peak value and average value of TE of spur gear tooth surface are 0.0984 and 1.781 $\mu$ rad respectively, and that of 3D machinable tooth surface are 0.0701 and 1.393 $\mu$ rad respectively. The results verify that the 3D machinable tooth surface designed in this paper has better transmission performance than the spur gear tooth surface.

## 6 Conclusion

In this paper, a novel 3D conjugate tooth surface design method of HD with double-circular-arc tooth profile is proposed, and an HD kinematics model considering the FS coning deformation is established. The backlash distribution and loaded tooth contact characteristics of the designed 3D machinable tooth surface are verified by motion simulation and finite element analysis. The main conclusions are as follows:

(1) The proposed 3D conjugate tooth surface design method can obtain an internal gear pair composed of a CS with a spur gear tooth surface and a FS with a 3D machinable tooth surface. The internal gear pair can realize multi-tooth meshing and wider tooth surface contact area in HD.

(2) Through multi-section assembly and motion simulation, part of the tooth profile on each section of the machinable tooth surface is always in meshing contact state, and there is no meshing interference between the CS and FS gear teeth. The overall backlash distribution of the FS made up of all sections is more uniform and the fluctuation is small.

(3) Under the rated torque, 24% of the FS teeth are engaged in meshing, and more than 4/5 of the tooth surface in the axial direction carries the load. The contact patterns, maximum contact pressure and transmission error peak-to-peak value of the machinable tooth surface are 227.2%, 40.67%, and 71.24% of the spur gear tooth surface respectively, showing excellent transmission performance.

### Authors' Contributions

CS and FZ were in charge of the whole research; XL analyzed the transmission principle; XD and ZL were in charge of the finite element analysis. All authors read and approved the final manuscript.

### Authors' Information

Chaosheng Song, born in 1983, is currently a professor at Chongqing University, China. His main research interests include gear geometry design and tooth contact analysis.

Feihong Zhu, born in 1995, is currently pursuing the Ph.D. degree in mechanical design and theory with Chongqing University, China. His research interests include the precision gear transmission and gear efficiency analysis.

Xinzi Li, born in 1994, is currently pursuing the Ph.D. degree in mechanical design and theory with Chongqing University, China. His research interests include the precision gear transmission and tooth contact analysis.

Xuesong Du, born in 1970, is currently an associate professor at Chongqing University, China. His main research interests include mechanical design and mechanical system optimization analysis.

Zhifeng Liu, born in 1983, is currently an engineer at Hangzhou Advance Gearbox Group Co., Ltd, China. His research interests include the dynamics of gear systems, and the design of accurate transmission.

### Availability of data and materials

Not applicable.

### Competing Interests

The authors declare that they have no competing interests.

### Funding

The authors would like to thank the National Key R&D Program of China(2018YFB2001500) and the Key-Area Research and Development Program of Guangdong Province (2019B090917002).

## Acknowledgements

Not applicable.

## Author Details

The State Key Laboratory of Mechanical Transmissions, Chongqing University, Chongqing 400030, China, and Hangzhou Advance Gearbox Group Co., Ltd, Hangzhou 311203, China.

## References

- [1] H. Dong, Study of kinematics and meshing characteristic of harmonic gear drives based on the deformation function of the flexspline, Dalian university of technology, 2008.
- [2] Y. Eloy, G. Ignacio, F. Alfonso, Stress analysis of strain wave gear drives with four different geometries of wave generator, *Meccanica*, 55 (2020) 2285-2304.
- [3] X. Li, C. Song, Y. Yang, C. Zhu, D. Liao, Optimal design of wave generator profile for harmonic gear drive using support function, *Mechanism and machine theory*, 152 (2020) 103941.
- [4] H. Dong, D. Wang, K.-L. Ting, Kinematic effect of the compliant cup in harmonic drives, *Journal of mechanical design*, 133 (2011) 051004-051001.
- [5] H. Xin, Design for basic rack of harmonic drive with double-circular-arc tooth profile, *China Mechanical Engineering*, 22 (2011) 656-662.
- [6] F. Zhu, X. Du, C. Song, C. Zhu, Y. Yang, D. Liao, Design and analysis of space conjugate tooth profile of harmonic drive considering deformation of flexspline cup, *Journal of Central South University (Science and Technology)*, 51 (2020) 2471-2479.
- [7] Z. Yu, S. Ling, X. Wang, L. Wang, Study on tooth profile design of harmonic drive with deformation model of flexspline, *Meccanica*, 56 (2021) 1883-1904.
- [8] G. Chen, H. Li, Y. Liu, Double-arc harmonic gear profile design and meshing analysis for multi-section conjugation, *Advances in mechanical engineering*, 11 (2019) 1-14.
- [9] Y. Yang, J. Li, J. Wang, F. Zeng, Analysis of tooth profile modification and meshing characteristics of double arc harmonic drive, *IEEE*, 2021, pp. 268-273.
- [10] M. Majchrak, R. Kohar, S. Hrcek, F. Brumercik, The comparison of the amount of backlash of a harmonic gear system, *Tehnički vjesnik*, 28 (2021) 771-778.
- [11] Y. Yang, J. Wang, Q. Zhou, J. Zhu, W. Yang, Exact solution for conjugate profiles of zero backlash harmonic drives with elliptical cam wave generators, *Journal of Central South University (Science and Technology)*, 48 (2017) 3231-3238.
- [12] W. Wu, P. Yu, Y. Hou, New design, new process of harmonic drive with short flexspline and its experiment, *Journal of Harbin Institute of Technology*, 46 (2014) 40-46.
- [13] D. Liu, J. Xing, X. Chen, Spatial tooth profile design and simulation analysis of harmonic drive with involute tooth profile, *Computer Integrated Manufacturing Systems*, 21 (2015) 709-715.
- [14] J. Wang, X. Zhou, J. Li, K. Xiao, G. Zhou, Three dimensional profile design of cup harmonic drive with double-circular-arc common-tangent tooth profile, *Journal of Zhejiang University*, 55 (2016) 616-713.
- [15] X. Chen, Arc tooth profile design and simulation research of harmonic drive based on mesh backlash assessment, *Tiangong university*, 2012.
- [16] X. Zeng, J. Li, J. Wang, T. Tang, C. Li, Design and modification of harmonic double circular arc tooth profile based on finite element method, *Journal of Zhejiang University (Engineering Science)*, 55 (2021) 1548-1565.
- [17] S. Wang, G. Jiang, X. Mei, C. Zou, X. Zhang, H. Zhang, A rapid stress calculation method for short flexspline harmonic drive, *Engineering computations*, 36 (2019) 1852-1867.

- [18] B.S. Mahanto, V. Sahoo, R. Maiti, Effect of cam insertion on stresses in harmonic drive in industrial robotic joints, *Procedia computer science*, 133 (2018) 432-439.
- [19] A. Fitzgibbon, M. Pilu, R.B. Fisher, Direct least square fitting of ellipses, *IEEE transactions on pattern analysis and machine intelligence*, 21 (1999) 476-480.
- [20] G. Jiang, S. Wang, X. Mei, X. Zhang, H. Zhang, Bidirectional conjugate design method for double-circular-arc tooth profile of harmonic drives, *Journal of Xi'an Jiaotong University*, 53 (2019) 8-14.